Highlights

Can spinodal decomposition occur during decompression-induced vesiculation of magma?

Mizuki Nishiwaki

- Vesiculation of magma during decompression was interpreted by simple thermodynamics.
- Binodal and spinodal curves of silicate–water systems were drawn versus pressure.
- Vesiculation of magma occurs by nucleation, not by spinodal decomposition.
- Supersaturation dependence of the bubble nucleus' surface tension was revisited.
- Estimation of surface tension by nonclassical nucleation theory remains difficult.

Can spinodal decomposition occur during decompression-induced vesiculation of magma?

Mizuki Nishiwaki[a,]

[a]*Center for Glass Science & Technology, School of Engineering, The University of Shiga Prefecture, 2500, Hassaka-cho, Hikone, Shiga, 522-8533, Japan*

Abstract

Volcanic eruptions are driven by decompression-induced vesiculation of supersaturated volatile components in magma. The initial phase of this phenomenon has long been described as a phase of nucleation and growth. Recently, it was proposed that spinodal decomposition (an energetically spontaneous phase separation that does not require the formation of a distinct interface) may occur during decompression-induced magma vesiculation. This suggestion has attracted considerable attention and is currently only based on qualitative textural observations of decompression experiment products (the independence of bubble number density on decompression rate; the homogeneous spatial distribution of the bubbles). In this study, I used a simple thermodynamic approach to quantitatively investigate whether spinodal decomposition can occur during the decompression-induced vesiculation of magma. I drew the binodal and spinodal curves for each magma on the chemical composition-pressure plane by approaching hydrous magmas at several conditions of temperature and chemical composition as two-component symmetric regular solutions of silicate and water, and using experimentally determined values of water solubility in these magmas. The spinodal curve was much lower than the binodal curve for all the magmas at pressures sufficiently below the second

Email address: nishiwaki.m(at)mat.usp.ac.jp (Mizuki Nishiwaki)

URL: https://sites.google.com/view/mizuki-nishiwaki (Mizuki Nishiwaki)

critical endpoint ($\lesssim$ 1000 MPa). In addition, the final pressure of all the decompression experiments performed to date fell between these two curves. This suggests that spinodal decomposition is unlikely to occur in the pressure range of magmatic processes in the continental crust or at realistic decompression rates, and that decompression-induced magma vesiculation results from nucleation, as previously suggested. To test this thermodynamic approach, I estimated the 'microscopic' surface tension between the melt and the bubble nucleus in previous decompression experiments by substituting the pressure of the spinodal curve into the equation for the dependence of surface tension on the degree of supersaturation. The resulting values were significantly more scattered than those obtained by the conventional method of inversion of the experimental bubble number density using the classical nucleation theory formula. Therefore, it is difficult to judge whether the equation of surface tension as a factor of supersaturation (based on the nonclassical nucleation theory) is appropriate for magma systems. Further careful consideration should be given to both experimental and theoretical aspects of magma vesiculation.

Keywords: hydrous magma, decompression-induced vesiculation, nucleation, spinodal decomposition, symmetric regular solution, surface tension

---

1. Introduction

Magma degassing is one of the strongest controlling factors in the dynamics of volcanic eruptions. Specifically, it is the decompression-induced vesiculation of volatiles (e.g., H_2O, CO_2, H_2S) originally dissolved in magma deep underground, that is, phase separation into silicate melt saturated with volatiles and volatile vapor saturated with trace amounts of silicate. The initial stage has long been understood as nucleation and growth (e.g., Shimozuru et al., 1957; Murase and McBirney, 1973; Sparks, 1978), and theoretical numerical models were constructed by Toramaru (1989, 1995) to predict the bubble number density (BND) based on classical nucleation theory (CNT, e.g., Hirth et al., 1970). In addition, in the last 30 years since the innovative work by Hurwitz and Navon (1994), many experiments have been conducted to reproduce decompression-induced vesiculation of mainly water-dissolved (hydrous) magmas in laboratory experimental

systems with controlled decompression rates. As data from decompression experiments to date generally agreed with numerical predictions (BND $\propto$ |decompression rate|$^{1.5}$ by Toramaru, 1995) based on CNT, Toramaru (2006) constructed the BND decompression rate meter (BND DRM). This theoretical model has been used extensively to estimate magma's decompression rate in a volcanic conduit based on quantitative analysis of the bubble texture of natural pyroclastic products, such as pumice.

However, some laboratory experiments performed thus far have reported results that are anharmonic to the above equations; Allabar and Nowak (2018) performed decompression experiments on hydrous phonolitic melts over a wide range of decompression rates, including 0.024–1.7 MPa/s, and obtained results independent of high BND values (5.2 mm^{-3}). To explain this result, they proposed a scenario in which spinodal decomposition, rather than nucleation as used in previous explanations, occurs in the early stages of decompression-induced vesiculation. Spinodal decomposition is the phase separation of a multi-component mixed or solid solution due to energetic instability (e.g., Cahn and Hilliard, 1959; Cahn, 1965). If the sign of the second-order derivative of the system's molar Gibbs energy of mixing Δg^{mix} with the chemical composition is positive, the system is metastable, and nucleation occurs, with distinct phase boundaries (interfaces) appearing spatially random. Conversely, if the sign is negative, the system is unstable, and spinodal decomposition occurs, wherein the two phases separate at a certain wavelength and the phase boundary remains unclear. Nucleation is downhill diffusion, whereas spinodal decomposition is uphill diffusion. In Allabar and Nowak (2018), spinodal decomposition was proposed for two reasons: (1) the timescale for spinodal decomposition in gas–liquid systems is much shorter than the timescale for decompression (Debenedetti, 2000), which could explain no dependence of BND on the decompression rate. (2) The spatial distribution of the bubbles in the experimental products was homogeneous, that is, they appeared to phase-separate at a given wavelength. Subsequent work by Sahagian and Carley (2020) raised the problem that "the surface tension between the melt and the very small bubble nucleus should act to push dissolved volatiles back into the melt, but bubbles of such size are still formed" as the "tiny bubble paradox." They extended the ideas of Allabar and Nowak (2018) as follows: if spinodal decomposition—rather than nucleation—occurs, this paradox can be resolved because interface formation is no longer necessary and explains the homogeneous spatial distribution of bubbles observed in some laboratory products.

Thus, the new theory that "decompression-induced vesiculation of magma can occur not only by nucleation but also by spinodal decomposition" has been actively discussed and has attracted much attention in the last six years. Gardner et al. (2023) also stated that future interpretations of BND and bubble size distributions of natural volcanic products must consider the possibility that various mechanisms of bubble formation may occur, including nucleation (homogeneous and heterogeneous) and spinodal decomposition. However, the discussion on spinodal decomposition has remained qualitative, and it is unclear whether spinodal decomposition actually occurs during decompression-induced magma vesiculation. Nonetheless, owing to the small spatiotemporal scale of the physical phenomena under investigation, it is likely to be extremely difficult to confirm via laboratory observational experiments such as in situ X-ray radiography. Therefore, in this paper, I quantitatively discuss which nucleation or spinodal decomposition mechanism occurs during decompression-induced magma vesiculation, based on a simple thermodynamic approach.

This study first reviews the thermodynamic definitions of nucleation and spinodal decomposition. Spinodal decomposition, which has traditionally been treated only when it occurs with temperature change at a constant pressure, can also be treated with pressure change at a constant temperature. It attempts to consider hydrous magmas in a simplified way as a symmetric regular solution of silicate and water and to quantitatively draw binodal and spinodal curves on the chemical composition–pressure plane using a simple calculation. Based on the results, I then discuss whether spinodal decomposition can occur during decompression-induced vesiculation of magma and give the author's views on the arguments in previous related papers. Finally, the above results are applied to calculate the "microscopic" surface tension between the melt–bubble nucleus using the the non-CNT equation proposed by Gonnermann and Gardner (2013). Finally, I present a personal perspective on the future direction of microscopic surface tension research.

2. What is spinodal decomposition?

2.1. Energetics of phase separation

Notations used in this study are listed in Table 1. If the mole fraction of one of the components is x ($0 < x < 1$) and the interaction parameter between the two components, which represents the non-ideality of mixing,

is w, then the molar Gibbs energy of mixing Δg^{mix} for a two-component symmetric regular solution can be expressed as follows:

$$\Delta g^{\mathrm{mix}} = \mathcal{R}T\{x \ln x + (1-x)\ln(1-x)\} + x(1-x)w. \tag{1}$$

In mixed systems with a miscibility gap, w is positive and the Δg^{mix} curve has two troughs, as shown in the upper panel of Fig. 1. When the temperature T and pressure P change, the system is metastable in the interval where the Δg^{mix} curve is convex downwards, that is, the sign of the second-order derivative with x is positive, and nucleation occurs with distinct phase boundaries (interfaces) appearing randomly in space. Conversely, in the interval where the Δg^{mix} curve is convex upward, that is, where the sign of the second-order derivative with x is negative, the system is unstable, and spinodal decomposition occurs wherein the two phases separate at a certain wavelength without a clear phase boundary.

$$\left(\frac{\partial \Delta g^{\mathrm{mix}}}{\partial x}\right)_{T,P} = \mathcal{R}T \ln\left(\frac{x}{1-x}\right) + (1-2x)w = 0, \tag{2}$$

$$\left(\frac{\partial^2 \Delta g^{\mathrm{mix}}}{\partial x^2}\right)_{T,P} = \frac{\mathcal{R}T}{x(1-x)} - 2w = 0. \tag{3}$$

Binodal and spinodal curves appear on the cut surfaces of binodal and spinodal surfaces in temperature–pressure–chemical composition space (e.g., Aursand et al., 2017). Hence, either temperature or pressure can be selected for the vertical axis in the lower panel of Fig. 1. Hereafter, we denote the x values that satisfy Eqs. (2) and (3) as x_{bi} and x_{spi}, respectively. In other words, x_{bi} and x_{spi} are the x values that constitute the binodal and spinodal curves, respectively.

2.2. The relation between binodal and spinodal curves

Although x and w inherently vary with temperature and pressure, they are treated here as functions $x_{\mathrm{bi}}(P), x_{\mathrm{spi}}(P)$, and $w(P)$, which depend only on pressure, assuming that temperature is constant. Combining Eqs. (2) and (3) and eliminating w, the following relation between x_{bi} and x_{spi} is derived:

$$x_{\mathrm{spi}} = \frac{1}{2}\left\{1 - \sqrt{1 - \frac{2(1-2x_{\mathrm{bi}})}{\ln\dfrac{1-x_{\mathrm{bi}}}{x_{\mathrm{bi}}}}}\right\}. \tag{4}$$

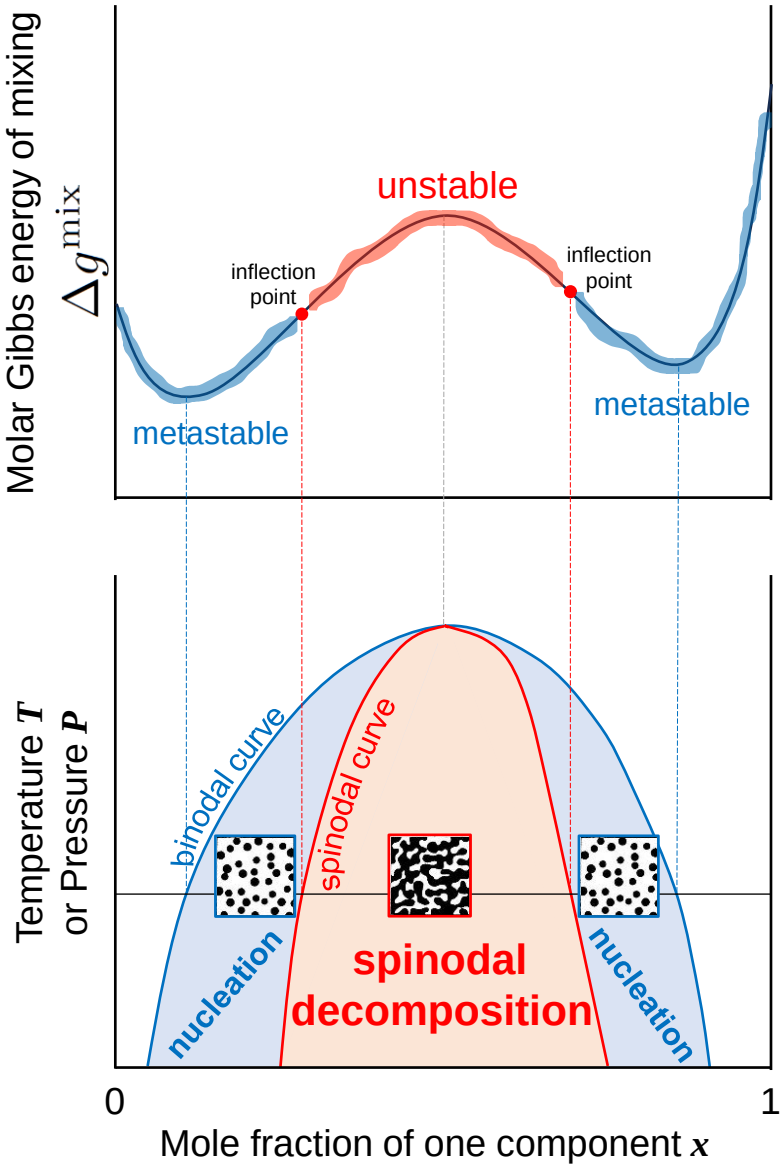

Figure 1: Schematic molar Gibbs energy of mixing Δg^{mix} (upper panel) and corresponding phase diagram (lower panel) for a general two-component symmetric regular solution. In the interval where the Δg^{mix} curve is convex downwards, the system is metastable, and nucleation occurs with clear phase boundaries (surfaces) appearing randomly in space. On the other hand, when the Δg^{mix} curve is convex upward, the system is unstable and spinodal decomposition occurs, in which the two phases separate at a certain wavelength while the phase boundary remains indistinct. Note that the phase diagram's vertical axis can correspond to temperature T or pressure P.

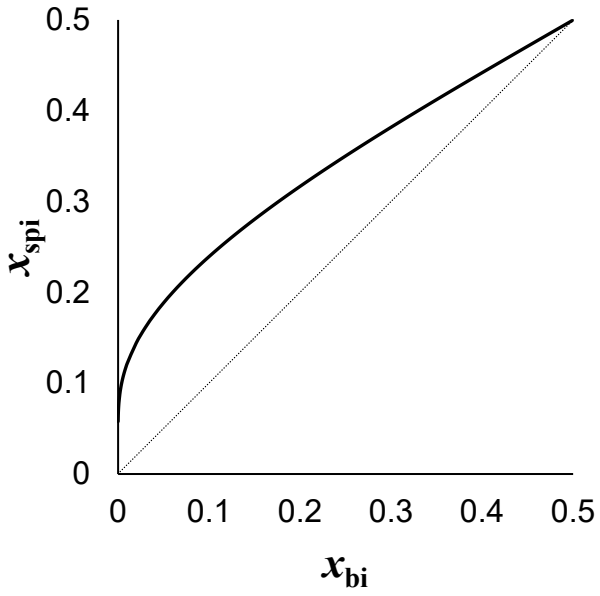

Figure 2: The relation between x_{bi} and x_{spi} at an arbitrary fixed temperature, derived from a series of Eqs. (2) and (3), which represent the first- and second-order derivatives of Δg^{mix} by x. x_{bi} and x_{spi} are the x values that constitute the binodal and spinodal curves, respectively. The range $0 < x < 0.5$ corresponds to the left half of Fig. 1. The relation $x_{\mathrm{spi}} > x_{\mathrm{bi}}$ holds for all the ranges.

This relation is shown in Fig. 2 in the $0 < x < 0.5$ range, corresponding to the left half area of Fig. 1.

2.3. Spinodal decomposition with pressure change

Since spinodal decomposition is a phenomenon discovered in the field of inorganic materials such as ceramics and alloys (e.g., Cahn, 1965), it is typically discussed in terms of phase separation into solid–solid/solid–liquid/liquid–liquid systems that occur with decreasing temperature at normal pressure. Thus, temperature is typically used as the vertical axis when drawing phase diagrams such as the one in the lower panel of Fig. 1. In contrast, when considering whether spinodal decomposition occurs in the phase separation of magma into gas–liquid systems, in this study, I assumed constant temperature and focused on the phase separation that occurs during decompression, since pressure decrease plays a much larger role than temperature increase as a cause of phase separation. Therefore, I adopted pressure as the vertical axis in the phase diagram in the lower

panel of Fig. 1. There are very few previous studies dealing with spinodal decomposition into gas–liquid systems in response to pressure changes, except for some studies on magmas (Gonnermann and Gardner, 2013; Allabar and Nowak, 2018; Sahagian and Carley, 2020; Gardner et al., 2023; Marks and Nowak, 2024; Hummel et al., 2024). Incidentally, when considering the phase separation of magma into a gas–liquid system by taking temperature as the vertical axis of the phase diagram, the diagram becomes a lower critical solution temperature (LCST) type phase diagram, in which the miscibility gap appears on the high-temperature side. Its direction is reversed from that of the phase diagram with pressure on the vertical axis. The next section 3.1 explains the interpretation of the mole fraction of mixing on the horizontal axis, i.e., it explains why magma can be treated as a two-component symmetric regular solution of silicate and water.

3. Binodal and spinodal curves in silicate–water systems

3.1. Thermodynamic assumptions

In this study, following Allabar and Nowak (2018), for simplicity, magma is treated as a symmetric regular solution composed of two components: silicate and water. Note that water in magma exists as two molecular species, the molecule H_2O_m and the hydroxyl group OH (e.g., Stolper, 1982a; 1982b), but we consider them together here. That is, x is the mole fraction of total water. In Fig. 1, the left end member ($x = 0$) corresponds to silicate and the right end member ($x = 1$) to water. Notably, at and near the silicate end member, a crystalline phase precipitates at low temperatures (e.g., Fig. 4 in Ostrovsky, 1966 for the SiO_2–H_2O system; Fig. 7 in Paillat et al., 1992; and Fig. 3 in Makhluf et al., 2020 for the albite–H_2O system); however, in this study, it is neglected assuming minute. Between each end member, namely, silicate and water, the binodal curve corresponds to hydrous melt and aqueous fluid, respectively. Thus, when a pressure change occurs that cuts the binodal curve at a fixed chemical composition, the reaction "magma (supercritical fluid) $\leftrightarrow$ water-saturated silicate melt (hydrous melt) + almost pure water vapor (aqueous fluid)" occurs. The rightward reaction indicates exsolution with decompression, whereas the leftward reaction indicates mutual dissolution with compression. For example, according to the results of high-temperature and high-pressure experiments shown in Fig. 3 of Makhluf et al. (2020), for the albite–water system at 900°C, the second critical endpoint (the vertex of the miscibility

gap) is in the range of 1.25–1.40 GPa and 42–45 wt%, i.e., $x = 0.57$–0.60 (on a single oxygen basis). Although the value of the mole fraction of water at the second critical endpoint can vary depending on the temperature and chemical composition of the silicate, in this study, it is assumed to be a symmetric regular solution, as it does not deviate significantly from $x = 0.5$ on a macroscopic scale at possible magma temperatures in the crust from the upper mantle (see Fig. 7 in Paillat et al., 1992); its dependence on systematic changes in the chemical composition of silicates has not been experimentally determined.

3.2. Calculation methods

The section for $x < 0.5$ of the binodal curve on the x–P plane at constant T, shown in the lower panel of Fig. 1, should coincide with the solubility curve of water in the silicate melt at that temperature with respect to pressure change. In other words, the water solubility $c(P)$ in the silicate melt is equal to $x_{\mathrm{bi}}(P)$, which constitutes the binodal curve. From this and the relation Eq. (4) between x_{bi} and x_{spi} shown in Section 2.2, we can calculate the value of x_{spi} that constitutes the spinodal curve. The value of the silicate–water interaction parameter $w(P)$ can also be determined by substituting the value of $x_{\mathrm{bi}}(P)$ into Eq. (2).

3.3. Conditions on the temperature, chemical composition, and water solubility in magma

Three types of silicate melts are assumed for temperature and chemical composition: K-phonolitic melt at 1050°C, basaltic melt at 1100°C, and albite melt at 900°C. For the phonolitic melt, the conditions are the same as those used in all experiments of Allabar and Nowak (2018). Basaltic and albite melts were chosen to compare and examine the spinodal curves' behavior at higher pressures. The temperatures employed are those at which the pressure dependence of water solubility in the melt is systematically determined from experiments. According to Iacono-Marziano et al. (2007), who performed decompression experiments using AD79 Vesuvius pumice as did Allabar and Nowak (2018), since the water solubility in K-rich phonolitic melt at 1050°C agrees well with the value calculated from the empirical model of Moore et al. (1998), their formula was also used in this study in the range 0.1–300 MPa. Note that Moore et al. (1998) defined the mole fraction of water by treating each oxide (e.g., SiO_2 and Al_2O_3) as one unit, but this definition is no longer in common use, and here, the mole fraction

was converted to the currently commonly used single-oxygen basis values (see Section 1.2 in Zhang, 1999). The water solubility in the basaltic melt at 1100°C was obtained by digitizing the fitting curve of the experimentally determined values for $\lesssim$ 600 MPa, as shown in Fig. 2 of Hamilton et al. (1964). The water solubility in the albite melt at 900°C was obtained by digitizing the fitting curve of the experimentally determined values for $\lesssim$ 1000 MPa, as shown in Fig. 8 of Burnham and Jahns (1962).

4. Calculation results

The binodal and spinodal curves drawn on the x–P plane for the three silicate–water systems are shown in Fig. 3. The geometric characteristics of both curves are similar, regardless of the silicate composition. Fig. 6 in Allabar and Nowak (2018) and Fig. 1 in Sahagian and Carley (2020) show a conceptual phase diagram in which both the binodal and spinodal curves are convex upward over the entire chemical-composition range, with a large area inside the spinodal curve. The lower panel of Fig. 1 in this study is identical. However, when considering their actual position and shape quantitatively based on chemical thermodynamics, the solubility curve (= binodal curve) is convex downward at $\lesssim$ 400 MPa (approximately the relation $c(P) \propto P^{0.5}$ holds); therefore, the spinodal curve is also convex downward. In the pressure range examined in this study, the spinodal curve is situated at a much lower pressure relative to the binodal curve when fixed at a certain water content. For example, at $x = 0.10$, the (water solubility (wt%), P_{bi} (MPa), P_{spi} (MPa)) for the phonolitic melt, basaltic melt, and albite melt are (5.4, 219, < 1), (5.2, 239, 6), and (5.8, 166, 10), respectively. Furthermore, as x increases, the corresponding P_{spi} gradually transitions to the high-pressure side, but the difference from P_{bi} is still very large. In other words, the nucleation region is much wider than the spinodal decomposition region, at least in the $x < 0.25$ range plotted in Fig. 3. For example, in the case of albite melt, $P_{\mathrm{bi}} = 1000$ MPa, which corresponds to approximately $P_{\mathrm{spi}} = 190$ MPa.

The calculation results for $w(P)$ are shown in Fig. 4. Although w is large at 0.1 MPa (phonolite: 75 kJ/mol, basalt: 85 kJ/mol, and albite: 95 kJ/mol), for all three chemical compositions it monotonically decreases rapidly with increasing pressure over the entire pressure range. This is consistent with the fact that the mutual dissolution of silicate and water proceeds at higher pressures, which narrows the miscibility gap.

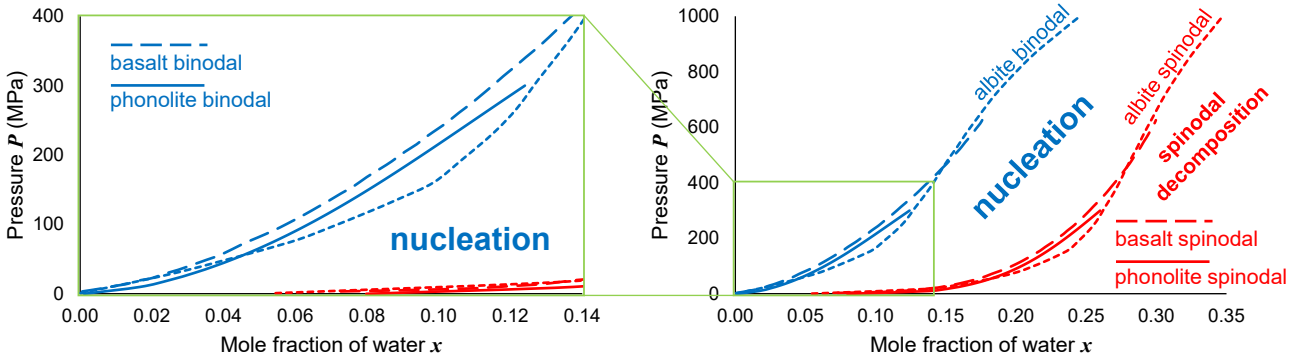

Figure 3: Binodal (blue) and spinodal (red) curves for hydrous 1050°C K-phonolitic (solid line), 1100°C basaltic (dashed line), and 900°C albite (dotted line) melts in the pressure range 0.1–1000 MPa. The left panel shows an enlargement of the right panel at pressures below 400 MPa. The binodal curves correspond to the water solubility curves in the melt for each chemical composition (Moore et al., 1998; Hamilton et al., 1964; Burnham and Jahns, 1962). The position of spinodal curves was determined from the position of binodal curves and Eq. (4).

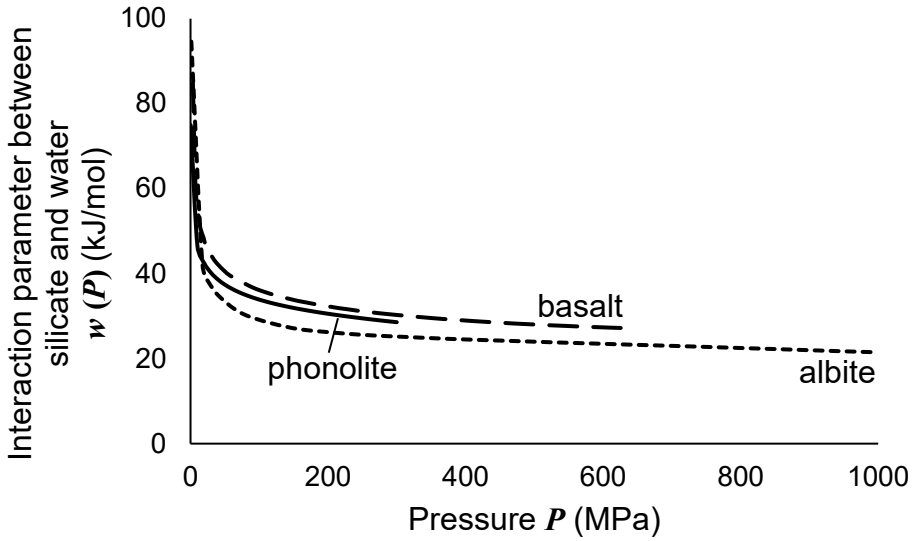

Figure 4: Calculation results of the interaction parameter between silicate and water $w(P)$ for hydrous K-phonolitic melt at 1050°C and 0.1–300 MPa (solid line), basaltic melt at 1100°C and 0.1–625 MPa (dashed line), and albite melt at 900°C and 0.1–1000 MPa (dotted line).

5. Discussion

5.1. Can spinodal decomposition occur during decompression-induced vesiculation of magma?

All nucleation pressure values in 88 previous laboratory experiments–from Gardner et al. (1999) to Le Gall and Pichavant (2016)–compiled and calculated by Shea (2017), fall within the nucleation region shown in Fig. 3 if variations in melt chemical composition are not considered. Additionally, all Allabar and Nowak (2018) experimental runs were performed in the range of the initial pressure of 200 MPa to final pressures of 70–110 MPa. Since the final pressure is higher than P_{spi}, the nucleation pressure of these runs inevitably falls into the nucleation region. Therefore, the innovative scenario proposed by Allabar and Nowak (2018) and Sahagian and Carley (2020), i.e., "spinodal decomposition during decompression-induced vesiculation of magma," cannot occur in the pressure range of magmatic processes in the continental crust at depths of several hundred MPa. In addition, since $P_{\mathrm{spi}} << P_{\mathrm{bi}}$ as shown in Fig. 3, for spinodal decomposition to occur without nucleation in the P–x range, it is necessary to maintain sufficient supersaturation, despite a very large decompression from an initial pressure higher than P_{bi} to a pressure lower than P_{spi}, which requires an unrealistically large decompression rate of at least several hundred MPa/s. Whereas Gardner et al. (2023) stated that we must consider the overlap of various bubble formation mechanisms, including spinodal decomposition, to interpret BND and bubble size distributions in natural pyroclasts, I argue that we can focus only on homogeneous and heterogeneous nucleation as before.

Of course, in regions of higher pressure and higher water content outside the drawn area of Fig. 3, P_{spi} asymptotically approaches P_{bi}, and spinodal decomposition is more likely to occur. In other words, if decompression occurs such that it passes near the top of the binodal curve (second critical endpoint, corresponding to high pressure in the upper mantle and a chemical composition of $x \simeq 0.5$), spinodal decomposition may occur. In addition, because the second critical endpoint of silicate–water systems has been reported to shift to lower temperatures and pressures with increasing amounts of alkali metal oxides (e.g., Na_2O and K_2O) in the silicate (Bureau and Keppler, 1999; Sowerby and Keppler, 2002), Allabar and Nowak (2018) suggested that spinodal decomposition at low pressures may be more likely to occur in alkali-rich phonolite melts than in other silicic silicates. However, as long as the symmetric regular solution approximation is assumed, the shift

of the second critical endpoint to lower pressures, i.e., the shift of the binodal curve to lower pressures, is accompanied by a shift of the spinodal curve to lower pressures because x_{bi} and x_{spi} change in tandem, as shown in Fig. 2. In this case, the region of spinodal decomposition shown in Fig. 3 would be narrower and spinodal decomposition would be less likely to occur. Therefore, if spinodal decomposition occurs in the phonolitic melt, the binodal curve of the phonolite–water system is expected to have a highly asymmetric shape to which the symmetric regular solution approximation cannot be applied. This might be related to the effective ionic radius of potassium (1.38 Å) that is abundant in the phonolitic melt and is as large as that of oxygen (1.40 Å) (Shannon, 1976). The packing ratio is higher than that in alkali-poor silicates (e.g., albite and rhyolite). Still, the shape of the binodal curve of the phonolite-water system has yet to be determined and requires exploration in detail using high-temperature and high-pressure experiments in the future.

5.2. On the manner of compiling experimental results by Allabar and Nowak (2018)

Allabar and Nowak (2018) added selected data from previous decompression experiments (Iacono-Marziano et al., 2007; Marxer et al., 2015; Preuss et al., 2016) conducted under the same chemical composition and physical conditions (phonolitic melt, 1050°C, initial pressure 200 MPa, and continuous decompression) to reinforce their newly obtained experimental data and plotted them on the decompression rate–BND plane (Fig. 8 in their paper), claiming that the BND is almost independent of the decompression rate. The BND values of the data selected were all in the same order of magnitude as the high BND values of the experimental data obtained by Allabar and Nowak (2018).

However, as Fig. 5 shows, for all four papers, even low BNDs were measured by Iacono-Marziano et al. (2007) and Marxer et al. (2015). In Iacono-Marziano et al. (2007), the variation in the BND for the same decompression rate is so large that it is not mentioned here. In Marxer et al. (2015), the BND increased with increasing decompression rate, which seems to be in harmony with the original BND DRM of Toramaru (2006) (see also Fig. 4 in Fiege and Cichy, 2015). In other words, the trends of the dependence of the BND on the decompression rate are quite different between the reports by Marxer et al. (2015) and those by {Preuss et al. (2016) and Allabar and Nowak (2018)}. However, the experiments were performed under almost identical conditions. While Allabar and Nowak (2018) focused only

on the high-value BND data that did not depend on the decompression rate and proposed spinodal decomposition to explain the discrepancy from BND DRM, I think we should first consider the causes of the discrepancy between the findings reported by Marxer et al. (2015) and those by {Preuss et al. (2016) and Allabar and Nowak (2018)} data, rather than jumping to such a novel idea.

Moreover, assuming that all the experimental results plotted in Fig. 5 are correct, they suggest that the decompression rate dependence of BND in phonolitic melts is extremely varied. It is known from magma crystallization experiments that the crystal number density can depend on the cooling rate (proportional to the 3/2 power of the cooling rate; consistent with the CNT-based prediction assuming diffusion-limited growth) as in Toramaru (2001) or shows no dependence, or even decreases (Martel and Schmidt, 2003; Cichy et al., 2011; Andrews and Befus, 2020). Toramaru and Kichise (2023) proposed that this wide range of cooling rate dependence can be explained by varying the pre-exponential factor of the nucleation rate and the surface tension. If there were a bubble version of this crystallization model, it might be possible to explain the wide variety of decompression rate dependence of BND.

5.3. On the "microscopic" surface tension between the melt and bubble nucleus

5.3.1. Supersaturation dependence of the surface tension: the suggestion by Gonnermann and Gardner (2013)

As discussed thus far, the theory of "spinodal decomposition during decompression-induced vesiculation of magma" proposed by Allabar and Nowak (2018) and Sahagian and Carley (2020) was rejected because it is unlikely to occur at the naturally realizable magma decompression rate. Notably, one of the remarkable properties of spinodal decomposition is that there is no "microscopic" surface tension between the melt and vapor (bubble nucleus) ($\sigma = 0$), as this process does not require the creation of a new interface. This idea connects smoothly on the phase diagram with the idea based on the non-CNT discussed by Gonnermann and Gardner (2013) that the greater the supersaturation, the lower the surface tension (Fig. 6).

In this section, I differentiate the surface tension based on the size scale of interest: in the case of a homogeneous spherical bubble nucleus, I call it the "microscopic" surface tension σ. Although σ is a very strong parameter governing nucleation, its direct measurement is currently still impossible;

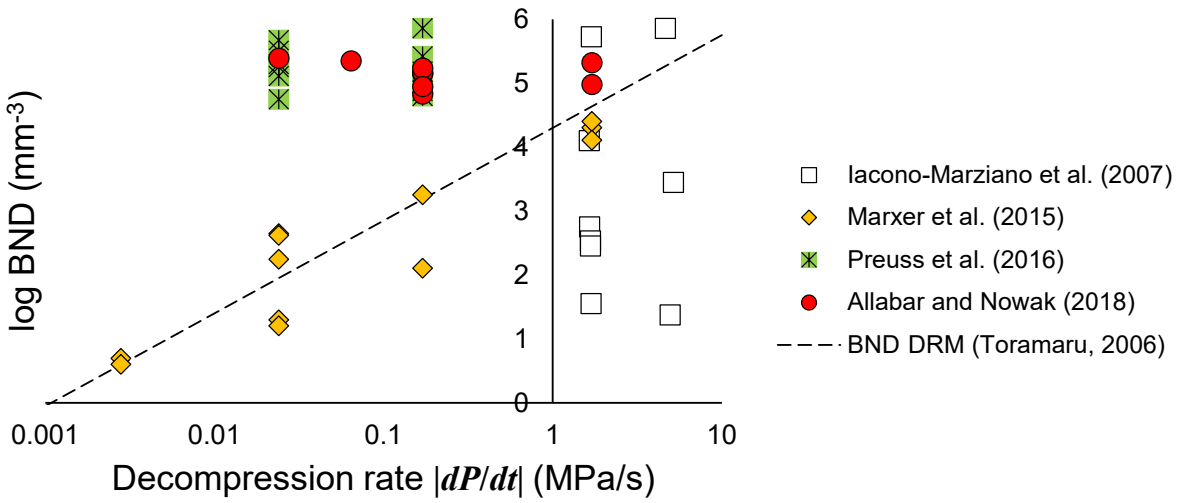

Figure 5: Results of decompression experiments using hydrous K-phonolitic melt from previous works (Iacono-Marziano et al., 2007; Marxer et al., 2015; Preuss et al., 2016; Allabar and Nowak, 2018). BND DRM means bubble number density decompression rate meter. The dotted line is the theoretical prediction calculated by BND DRM from Toramaru (2006).

therefore, it has been calculated only by fitting the integrated value of the CNT-based nucleation rate J over time with the obtained BND from decompression experiments (the inversion of BND using the CNT formula) (e.g., Mourtada-Bonnefoi and Laporte, 2004; Cluzel et al., 2008; Hamada et al., 2010; Shea, 2017). See Appendix A for the detailed expression of the equation of J in CNT (e.g., Hirth et al., 1970). On the other hand, in the case of a flat interface, I call it the "macroscopic" surface tension σ_∞. There are only a few examples of direct measurements of σ_∞, and the measurements by Bagdassarov et al. (2000) are widely used. In BND DRM (Toramaru, 2006), a theoretical model for estimating magma decompression rates using values of BND and several physical property parameters (e.g., the diffusion coefficient of water in the melt, viscosity coefficient of the melt, and surface tension) obtained from microtextural analyses of natural pyroclasts, the capillary approximation has been applied to ignore the curvature at the melt-bubble nucleus interface, i.e. assuming it is flat. In other words, it has been assumed that $\sigma = \sigma_\infty$.

Contrary to this approximation, it has been found that σ obtained via the CNT formula tends to be significantly smaller than σ_∞ (e.g., Hamada

et al., 2010). Gonnermann and Gardner (2013) attributed this discrepancy to applying the capillary approximation, which is strictly valid only near equilibrium, to a non-equilibrium melt-bubble nucleus system with large supersaturation. According to the recent non-CNT, the interface between the original and new phases loses sharpness and diffuses under non-equilibrium conditions (e.g., Chapter 4 in Kelton and Greer, 2010). In other words, such interfacial diffusion should also occur during the vesiculation of magma with supersaturated water, which is no longer soluble due to decompression.

Based on the non-CNT, they considered a situation where σ depends on the degree of supersaturation: the greater the degree of supersaturation, the smaller σ becomes. When the "spinodal limit" far from equilibrium is reached, σ is zero. This can be reinterpreted in the chemical composition–pressure plane phase diagram at constant temperature drawn in this study, as shown in Fig. 6. Decompression corresponds to the decrease in the melt pressure P_{M} and the increase in the degree of supersaturation, which passes through the following three points as it progresses:

1) Blue point: The saturation pressure P_{SAT} is the pressure on the binodal curve (= binodal pressure P_{bi}), and the degree of supersaturation is 0. If phase separation occurs at this point, nucleation occurs, and the interface between the melt and bubble nucleus is sharp and clear ($\sigma = \sigma_\infty$).

2) Black point: The supersaturation increases as the pressure drops through the nucleation region between the binodal and spinodal curves. If phase separation occurs at this point, nucleation occurs; however, the interface between the melt and bubble nucleus loses sharpness and diffuses, and σ becomes lower than that in 1) ($\sigma < \sigma_\infty$).

3) Red point: When reaching the spinodal curve (= spinodal pressure P_{spi}), the degree of supersaturation reaches maximum in the nucleation region. At pressures below this point, spinodal decomposition occurs, where phase separation starts from the absence of an interface between the melt and bubble nucleus ($\sigma = 0$).

Gonnermann and Gardner expressed this physical situation (the dependence of the surface tension on the degree of supersaturation) in a mathematical formula. They used it to model the results of the decompression experiments. They claimed that the modeling showed that σ strongly depends on the degree of supersaturation and that its value is smaller than σ_∞. However, it should be noted that this logic seems to be self-contradictory. While their claims seemed as if they had discovered for the first time that the relation $\sigma < \sigma_\infty$ always holds as a result of the modeling,

which is a natural consequence, because prior to the modeling, the relation between σ and σ_∞ within the nucleation region had been defined as follows (the same as Eq. (17) in their paper). Here, ξ is an index of supersaturation, and its definition is presented in the next section 5.3.2.

$$\sigma = \sigma_\infty (1 - \xi^2)^{\frac{1}{3}} \qquad (0 \leq \xi \leq 1). \tag{5}$$

Nevertheless, despite this logical flaw, their idea is so groundbreaking that it is now worth reconsidering. If their ideas are correct, a relatively spinodal decomposition-like texture could emerge. For example, when supersaturation is large (i.e., when σ is small), the distance between bubbles would follow an almost constant wavelength, even though nucleation is occurring.

5.3.2. Estimation of the surface tension based on the nonclassical nucleation theory

Based on the above discussion, it is necessary to quantify the decrease in the microscopic surface tension σ with increasing supersaturation in the nucleation region to quantitatively investigate the role of bubble nucleation during decompression-induced magma vesiculation. This implies obtaining the specific value of an index of supersaturation ξ in Eq. (5), defined by Gonnermann and Gardner (2013) as follows:

$$\xi = \frac{P_{\mathrm{B}}^* - P_{\mathrm{M}}}{P_{\mathrm{B}}^* - P_{\mathrm{spi}}}, \tag{6}$$

where P_{B}^* is the internal pressure of a critical bubble nucleus. A bubble nucleus at the critical radius R_{c} satisfies mechanical and chemical equilibrium with the surrounding melt. The mechanical equilibrium is expressed as follows:

$$P_{\mathrm{B}}^* = P_{\mathrm{M}} + \frac{2\sigma}{R_{\mathrm{c}}}. \tag{7}$$

Note that Eq. (6) was formulated assuming that $P_{\mathrm{B}}^* = P_{\mathrm{M}}$ holds i.e. R_{c} diverges to ∞ (from Eq. (7)) on the binodal curve, that is, $\xi = 0$ ($\sigma = \sigma_\infty$). On the other hand, on the spinodal curve, it is $P_{\mathrm{M}} = P_{\mathrm{spi}}$, that is, $\xi = 1$ ($\sigma = 0$). The chemical equilibrium is expressed as follows:

$$f(T, P_{\mathrm{B}}^*) = f(T, P_{\mathrm{SAT}}) \exp\left\{ \frac{\overline{V}_{\mathrm{H_2O}}}{k_{\mathrm{B}} T} (P_{\mathrm{M}} - P_{\mathrm{SAT}}) \right\}, \tag{8}$$

where $f(T, P)$, the pure-water vapor fugacity at this temperature and pressure, can be obtained from the equation of state for water as a real

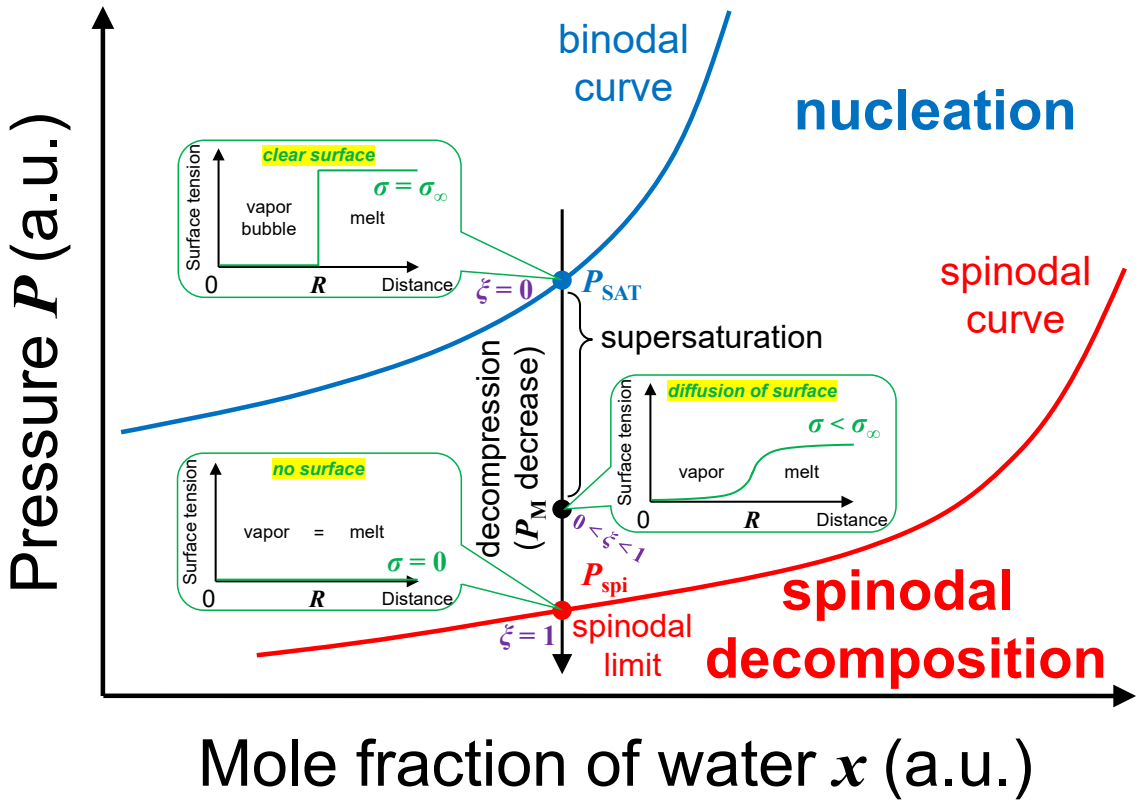

Figure 6: Schematic diagram of the change in the "microscopic" surface tension σ between the melt and vapor (bubble nucleus) with decreasing pressure, based on the nonclassical nucleation theory (Gonnermann and Gardner, 2013), in the phase diagram of the silicate–water system on the plane of mole fraction of water x–pressure P at constant temperature. Both vertical and horizontal axes have arbitrary units. The arrow indicates the decompression path, equivalent to the decrease of the melt pressure P_{M} and the increase of the degree of supersaturation. See Section 5.3.2 for the definition of ξ, the index of degree of supersaturation. The blue point on the binodal curve corresponds to the saturation pressure P_{SAT} and the degree of supersaturation is 0 ($\xi = 0$). At this point, nucleation occurs, where the interface between the melt and bubble nucleus is sharp and clear ($\sigma = \sigma_\infty$). The black point, where decompression has progressed, has some degree of supersaturation ($0 < \xi < 1$). During nucleation at this point, the interface between the melt and bubble nucleus loses sharpness and diffuses ($\sigma < \sigma_\infty$). The red point on the spinodal curve corresponds to the spinodal pressure P_{spi} and the degree of supersaturation reaches maximum within the nucleation region ($\xi = 1$). At pressures below this point, spinodal decomposition occurs, where phase separation starts from a state where the interface between the melt and bubble nucleus does not exist ($\sigma = 0$).

gas (e.g., IAPWS95 by Wagner and Pruß, 2002). $\overline{V}_{H_2O}$ is the partial molar volume of water in the melt and can be obtained from the regressed data in Ochs and Lange (1999). This equation (8) has been used for the determination of P_B^* since it was invented by Cluzel et al. (2008). The determined P_B^* values from Eq. (8) summarized in Shea (2017)'s Appendix table are relisted in Table 2. Gonnermann and Gardner (2013) assumed P_{spi} to be hypothetical and varied the numerator and denominator values on the right-hand side of Eq. (6) so that the experimental BND values could be reproduced. Here, in contrast, P_{spi} is a known parameter, and σ can be calculated from Eqs. (6) and (5).

I extracted the results of the single-step decompression (SSD) and homogeneous nucleation experiments (Gardner and Ketcham, 2011; Gardner, 2012; Gardner et al., 2013), summarized in Shea's (2017) Appendix table, and calculated σ corresponding to the experimental conditions of each run. SSD and homogeneous nucleation processes are simpler than continuous or multi-step decompression and heterogeneous nucleation; as such, they lend themselves to the application of the nucleation theory more readily than the latter two processes. The experimental conditions used for each run are listed in Table 2. In SSD, decompression to the final pressure is instantaneous; therefore, P_M can be regarded as equal to the final pressure, P_f.

To obtain σ, P_{spi} must be initially determined. P_{spi} is indeed calculable using Eq. (4) because the water solubility x_{bi} at P_{SAT} has been experimentally determined before the decompression experiments in most of the earlier studies. However, it is difficult to accurately determine P_{spi} as solubility measurement errors are often large. Furthermore, when comparing the P_{SAT} values in these decompression experiments (121–200 MPa) with Fig. 3 while ignoring the differences in temperature and chemical composition, all the P_{spi} values fall within the 0–10 MPa range. Therefore, P_{spi} was uniformly set to 5 MPa for convenience.

Table 2 and Fig. 7 show the values of the microscopic surface tensions σ calculated in this study and σ_{Shea} calculated by the conventional method (the inversion of BND using the CNT formula) in Shea (2017), and the macroscopic surface tension σ_∞ calculated using the empirical formula Eq. (1) in Hajimirza et al. (2019). The values of σ and σ_{Shea} were significantly lower than σ_∞–a result consistent with previous reports (e.g., Hamada et al., 2010). However, some of the σ values were higher, and others were lower than σ_{Shea}, and their variation was very large. Therefore, nothing can be said with certainty about the validity of the non-CNT-based equations (5)

and (6) proposed by Gonnermann and Gardner (2013) and, by extension, about the dependence of σ on supersaturation. This relationship should be carefully explored, both experimentally and theoretically, in the future.

Table 1: Notation list.

Symbol	Unit	Definition
a_0	m	Average distance between water molecules in the melt
c	no unit	Water solubility in the melt (mole fraction)
$D_{\mathrm{H_2O}}$	$\mathrm{m^2\ s^{-1}}$	Diffusivity of total water in the melt
f	Pa	Fugacity
J	$\mathrm{No\ m^{-3}\ s^{-1}}$	Nucleation rate
k_{B}	$\mathrm{J\ K^{-1}}$	Boltzmann's constant
n_0	$\mathrm{No\ m^{-3}}$	Number of water molecules per unit melt volume
P	Pa	Pressure
P_{bi}	Pa	Pressure on the binodal curve (= binodal pressure)
P_{f}	Pa	Final pressure of decompression experiments
P_{spi}	Pa	Pressure on the spinodal curve (= spinodal pressure)
P_{M}	Pa	Melt pressure
P_{SAT}	Pa	Water saturation pressure
P_{B}^*	Pa	Internal pressure of the critical bubble nucleus
R	m	Radius of a bubble nucleus
R_{c}	m	Critical bubble radius
$\mathcal{R}$	$\mathrm{J\ K^{-1}\ mol^{-1}}$	Gas constant
T	K	Temperature
$\overline{V}_{\mathrm{H_2O}}$	$\mathrm{m^3\ mol^{-1}}$	Partial molar volume of water in the melt
w	$\mathrm{J\ mol^{-1}}$	Interaction parameter between two components
x	no unit	Mole fraction of one of the two components
x_{bi} (P)	no unit	The x that constitutes the binodal curve at pressure P
x_{spi} (P)	no unit	The x that constitutes the spinodal curve at pressure P
δ_{T}	m	Tolman length
Δg^{mix}	$\mathrm{J\ mol^{-1}}$	Molar Gibbs energy of mixing
ξ	No	Index of supersaturation (overpressure) defined by Eq. (6)
σ	$\mathrm{N\ m^{-1}}$	"Microscopic" surface tension between the melt and homogeneous spherical bubble nucleus with a large curvature
σ_{Shea}	$\mathrm{N\ m^{-1}}$	σ calculated by inverting the bubble number density (BND) of decompression experiments using the classical nucleation theory (CNT) formula in Shea (2017)
σ_∞	$\mathrm{N\ m^{-1}}$	"Macroscopic" surface tension at the flat interface between the melt and vapor

Melt composition	SiO_2 (wt%)	Run#	T (°C)	P_{SAT} (MPa)	P_B^* (MPa)	P_M (MPa)	ξ (no unit)	σ (N/m)	σ_{Shea} (N/m)	σ_∞ (N/m)
rhyolite	76.53	G-1065[c]	1150	190.0	152.6	75.5	0.522	0.104	0.076	0.115
rhyolite	76.53	G-936[a]	1085	172.0	139.1	38.0	0.754	0.087	0.072	0.115
rhyolite	76.53	G-705[a]	975	162.0	128.1	40.0	0.716	0.086	0.070	0.109
rhyolite	76.53	G-608[a]	875	161.0	124.3	13.5	0.929	0.053	0.067	0.102
rhyolite	76.53	G-889[a]	825	154.0	119.1	8.5	0.969	0.039	0.064	0.100
rhyolite	76.53	G-740[a]	775	140.0	100.3	15.0	0.895	0.059	0.073	0.101
dacite	69.85	G-792[c]	1150	160.0	128.3	26.5	0.826	0.084	0.079	0.123
dacite	66.93	G-796[a]	1150	160.0	136.0	27.0	0.832	0.083	0.064	0.123
trachyte	62.57	G-1082[c]	1150	151.0	121.0	39.0	0.707	0.100	0.080	0.126
Na-phonolite	61.47	G-733[b]	1150	155.0	137.0	48.0	0.674	0.102	0.054	0.125
Na-phonolite	61.47	G-999[b]	875	121.0	101.0	21.0	0.833	0.078	0.055	0.115
basaltic andesite	54.12	G-1165[c]	1200	200.0	161.0	54.5	0.683	0.095	0.078	0.117
phonotephrite	51.13	G-1116[c]	1150	151.0	123.0	48.0	0.636	0.106	0.075	0.126

Table 2: Table 2: The surface tension values between the bubble nucleus and the surrounding melt correspond to each run of the previous single-step decompression (SSD) experiments for various chemical compositions and temperature conditions. All runs are those in which homogeneous nucleation appeared to occur, and were extracted from Shea's (2017) Appendix table. The corresponding references (a: Gardner and Ketcham, 2011; b: Gardner, 2012; c: Gardner et al., 2013) are indicated at the top right of the run number Run#. P_{SAT}: the saturation pressure; P_B^*: the internal pressure of the critical bubble nucleus calculated in Shea (2017) using Eq. (8); P_M: the melt pressure (equals to the final pressure of decompression P_f); ξ: the index of the degree of supersaturation defined by Eq. (6); σ: the microscopic surface tension between the melt and bubble nucleus, obtained in this study to confirm the validity of the supersaturation dependence equation originally discussed in Gonnermann and Gardner (2013); σ_{Shea}: the microscopic surface tension obtained by the conventional method—the inversion of BND using the classical nucleation theory (CNT) formula—in Shea (2017); σ_∞: the macroscopic surface tension at the flat melt–vapor interface, calculated from the empirical formula Eq. (1) in Hajimirza et al. (2019).

5.3.3. Future directions in microscopic surface tension research

As also explained by Fig. 2 in Shea (2017), σ is very poorly constrained, even though its importance for the estimation of the nucleation rate or decompression rate is much more significant than that of the other parameters. Constraining σ is key for achieving consistency between the results of magma decompression experiments and nucleation theory, and for further improving the ability of BND DRM to accurately estimate the decompression rate of natural magmas. Currently, a considerable number of BND data from decompression experiments significantly deviate from the values predicted by BND DRM (Fig. 4 in Fiege and Cichy, 2015). Moreover, BND DRM tends to overestimate decompression rates more than other methods (microlite number density, experiments, hornblende rims, seismicity, extrusion rate and diffusion rates) (Fig. 5 in Cassidy et al., 2018).

The dependence of σ on supersaturation was introduced in Section 5.3.1. In addition, Hajimirza et al. (2019) discussed the dependence of σ on another factor, the radius of a bubble nucleus R. This dependence is called the Tolman correction (Tolman, 1949) and is based on the following considerations: when the bubble size is very small (i.e., the interface curvature is large); as in nucleation, this geometric effect on the molecular interaction results in the relation that σ is less than σ_∞. The Tolman correction is expressed as follows:

$$\frac{\sigma}{\sigma_\infty} = \frac{1}{1 + 2\delta_\mathrm{T}/R}, \tag{9}$$

where δ_T is a length scale called the Tolman length. By applying this theory to the results of decompression experiments, Gardner et al. (2023) found that R and σ are large in conditions of strong supersaturation. This finding contradicts the supersaturation dependence described by Gonnermann and Gardner (2013). This contradiction remains unresolved.

In light of this discussion, I propose two ideas for future research on this topic:

1) To integrate the dependence of σ on the supersaturation and the bubble nucleus radius: As stated by Gardner et al. (2023), a constant Tolman length δ_T, the assumption imposed in Hajimirza et al. (2019), is only valid for small deviations from the thermodynamic equilibrium, and is likely to collapse as nucleation proceeds at a higher degree of supersaturation (Joswiak et al., 2013). In other words, δ_T appears to depend on the degree of supersaturation. This implies that the dependence of σ

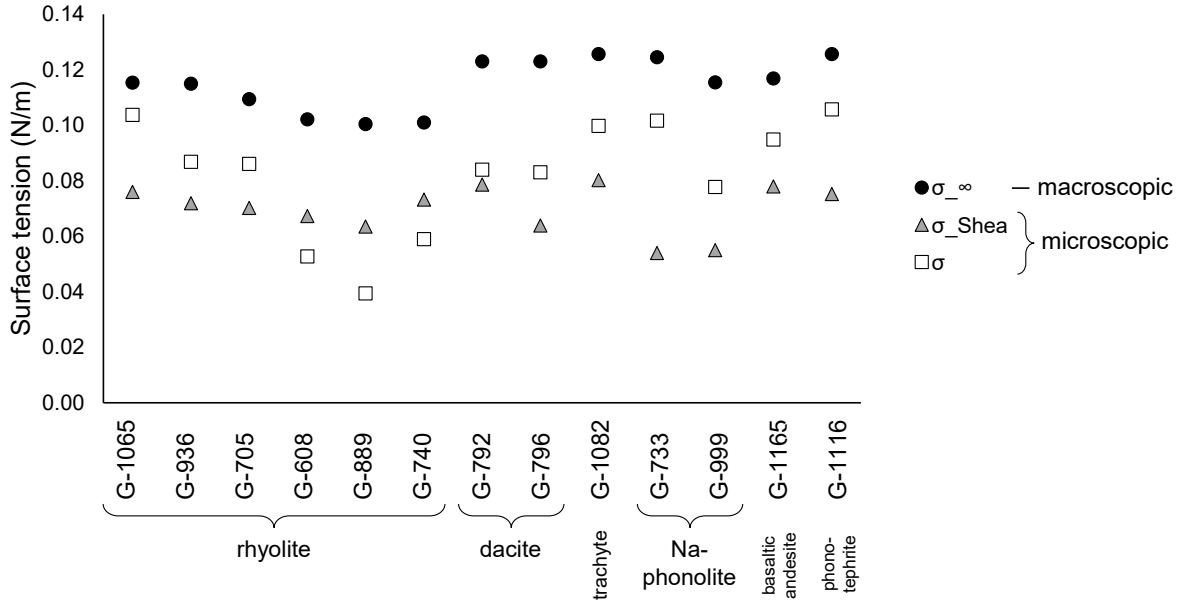

Figure 7: The "macroscopic" and "microscopic" surface tension values between the bubble nucleus and the surrounding melts of various chemical composition and temperature conditions, as shown in Table 2. For symbols, see Table 2.

on supersaturation and the bubble nucleus radius, which were considered separately, are interrelated. As shown in Eq. (7), the bubble radius is determined by the degree of supersaturation; therefore, these two factors should not be considered separately. As mentioned in Section 3.6.1 of Toramaru (2022), a higher-order Tolman correction (e.g., Schmelzer and Baidakov, 2016; Tanaka et al., 2016) should be applied since Eq. (9) used currently is only a first-order approximation.

2) To use data from high-temporal-resolution decompression experiments to estimate σ: specifically, it is expected that the time evolution of the BND can be investigated in detail in the case of SSD by varying the time after decompression to quench the collection of the experimental product. Thus, the time variation of J as a process of resolving the high supersaturation caused by the rapid decompression can be revealed with precision. In this regard, the work by Hajimirza et al. (2022) is the most detailed investigation of the BND at each time point after decompression and has yielded the most accurate J values between each time point to date. Their experimental results would provide the most reliable σ values to date in the series of attempts for its estimation by the inversion of BND using the CNT formula.

The discrepancy between the theoretical and experimental BND values may also be owing to reasons other than the surface tension. Preuss et al. (2016) mentioned that the diffusion coefficient of water should not be that of the total H_2O; instead it should be that of H_2O_m, which is an order of magnitude larger than that of H_2O. This would reduce the theoretical value of BND by an order of magnitude. Nishiwaki and Toramaru (2019) indicated that, when the viscosity of the melt is high, it suppresses nucleation. The BND in Toramaru's (1995) viscosity-controlled regime may be overestimated. Therefore, it is necessary to carefully evaluate the discrepancy between the theoretical and experimental BND values by revisiting the basic physical processes of magma vesiculation, reexamining how each physical property contributes to nucleation, and reassigning appropriate values to the physical property parameters.

6. Conclusions

I calculated the positions of the binodal and spinodal curves on the chemical composition-pressure plane by assuming that hydrous magma is a two-component symmetric regular solution of silicate and water and using the chemical thermodynamic equation and experimental data on water

solubility in magma. The spinodal curve was significantly lower than the binodal curve at pressures sufficiently below the second critical endpoint ($\lesssim$ 1000 MPa). The magmatic processes associated with volcanic eruptions in most natural continental crusts and the pressure ranges of all previous decompression experiments fell between these two curves. Therefore, decompression-induced vesiculation of magma occurs through nucleation, and spinodal decomposition is highly unlikely. This result contradicts the recent qualitative inference that spinodal decomposition can occur based on observations of the bubble texture of decompression-experimental products.

As an application of this thermodynamic approach, I estimated the "microscopic" surface tension between the melt and the bubble nucleus in previous decompression experiments by substituting the pressure of the spinodal curve into the equation that relates the surface tension to the degree of supersaturation (Gonnermann and Gardner, 2013). However, the surface tension values estimated by this method varied much more than those obtained by the conventional method (inversion of the bubble number density using the CNT formula). Therefore, the validity of this equation for a magma system based on the nonclassical nucleation theory is difficult to evaluate at this point and should be carefully tested, both experimentally and theoretically, in the future.

Appendix A. Equation of the nucleation rate in classical nucleation theory (CNT)

The equation for J in CNT (Hirth et al., 1970) is as follows:

$$J = \frac{2n_0^2 D_{\mathrm{H_2O}} \overline{V}_{\mathrm{H_2O}}}{a_0} \sqrt{\frac{\sigma}{k_{\mathrm{B}} T}} \exp\left\{ -\frac{16\pi\sigma^3}{3k_{\mathrm{B}}T} (P_{\mathrm{B}}^* - P_{\mathrm{M}}) \right\}, \tag{A.1}$$

where n_0 is the number of water molecules per unit volume, $D_{\mathrm{H_2O}}$ is the diffusivity of total water in the melt, $\overline{V}_{\mathrm{H_2O}}$ is the partial molar volume of water in the melt, a_0 is the average distance between water molecules in the melt, σ is the "microscopic" surface tension between the melt and the bubble nucleus, k_{B} is the Boltzmann's constant, T is the temperature, P_{B}^* is the internal pressure of the critical bubble nucleus, and P_{M} is the pressure of the melt.

Acknowledgments

The author is grateful to Yosuke Yoshimura at Kyoto University for discussing spinodal decomposition in gas–liquid systems induced by pressure changes. The author is grateful to Atsushi Toramaru at Kyushu University for his insightful comments on the similarity to the latest crystallization models, which contributed to enhancing the content of this paper. The author would like to thank Takeshi Ikeda at Kyushu University for many discussions on the fundamentals of the thermodynamics of silicate–water immiscibility. The reading circle for a glass science text with Shigeru Yamamoto at The University of Shiga Prefecture inspired the author for this study. Shumpei Yoshimura at Hokkaido University informed the author about some methods for calculating the mole fraction of water in magma. The content of this paper was deepened after the discussion with Hidemi Ishibashi at Shizuoka University. This work was supported by JSPS KAKENHI Grant Number JP23K19069. The author would like to thank Editage (www.editage.jp) for English language editing.

References

Allabar, A., and Nowak, M., 2018. Message in a bottle: Spontaneous phase separation of hydrous Vesuvius melt even at low decompression rates. *Earth Planet. Sci. Lett.* **501**, 192–201. https://doi.org/10.1016/j.epsl.2018.08.047

Andrews, B. J., and Befus, K. S., 2020. Supersaturation nucleation and growth of plagioclase: a numerical model of decompression-induced crystallization. *Contrib. Mineral. Petrol.* **175** (3), 1–20. https://doi.org/10.1007/s00410-020-1660-9

Aursand, P., Gjennestad, M. A., Aursand, E., Hammer, M., and Wilhelmsen, Ø., 2017. The spinodal of single- and multi-component fluids and its role in the development of modern equations of state. *Fluid Phase Equilib.* **436**, 98–112. https://doi.org/10.1016/j.fluid.2016.12.018

Bagdassarov, N., Dorfman, A., and Dingwell, D. B., 2000. Effect of alkalis, phosphorus, and water on the surface tension of haplogranite melt. *Am. Mineral.* **85** (1), 33–40. https://doi.org/10.2138/am-2000-0105

Bureau, H., and Keppler, H., 1999. Complete miscibility between silicate melts and hydrous fluids in the upper mantle: experimental evidence and geochemical implications. *Earth Planet. Sci. Lett.* **165** (2), 187–196. https://doi.org/10.1016/S0012-821X(98)00266-0

Burnham, C. W., and Jahns, R. H., 1962. A method for determining the solubility of water in silicate melts. *Am. J. Sci.* **260** (10), 721–745. https://doi.org/10.2475/ajs.260.10.721

Cahn, J. W., 1965. Phase separation by spinodal decomposition in isotropic systems. *J. Chem. Phys.* **42** (1), 93–99. https://doi.org/10.1063/1.1695731

Cahn, J. W., and Hilliard, J. E., 1959. Free energy of a nonuniform system. III. Nucleation in a two-component incompressible fluid. *J. Chem. Phys.* **31** (3), 688–699. https://doi.org/10.1063/1.1730447

Cassidy, M., Manga, M., Cashman, K., and Bachmann, O., 2018. Controls on explosive-effusive volcanic eruption styles. *Nat. Commun.* **9** (1), 1–16. https://doi.org/10.1038/s41467-018-05293-3

Cichy, S. B., Botcharnikov, R. E., Holtz, F., and Behrens, H., 2011. Vesiculation and microlite crystallization induced by decompression: a case study of the 1991–1995 Mt Unzen eruption (Japan). *J. Petrol.* **52** (7–8), 1469–1492. https://doi.org/10.1093/petrology/egq072

Cluzel, N., Laporte, D., Provost, A., and Kannewischer, I., 2008. Kinetics of heterogeneous bubble nucleation in rhyolitic melts: implications for the number density of bubbles in volcanic conduits and for pumice textures. *Contrib. Mineral. Petrol.* **156** (6), 745–763. https://doi.org/10.1007/s00410-008-0313-1

Debenedetti, P. G., 2000. Phase separation by nucleation and by spinodal decomposition: Fundamentals. In: Kiran, E., Debenedetti, P. G., Peters, C. J. (Eds.), Supercritical Fluids. Nato Science Series **366**, 123–166. https://doi.org/10.1007/978-94-011-3929-8_5

Fiege, A., and Cichy, S. B., 2015. Experimental constraints on bubble formation and growth during magma ascent: A review. *Am. Mineral.* **100** (11–12), 2426–2442. https://doi.org/10.2138/am-2015-5296

Gardner, J. E., 2012. Surface tension and bubble nucleation in phonolite magmas. *Geochim. Cosmochim. Acta* **76**, 93–102. https://doi.org/10.1016/j.gca.2011.10.017

Gardner, J. E., and Ketcham, R. A., 2011. Bubble nucleation in rhyolite and dacite melts: temperature dependence of surface tension. *Contrib. Mineral. Petrol.* **162** (5), 929–943. https://doi.org/10.1007/s00410-011-0632-5

Gardner, J. E., Hilton, M., and Carroll, M. R., 1999. Experimental constraints on degassing of magma: isothermal bubble growth during continuous decompression from high pressure. *Earth Planet. Sci. Lett.* **168**

(1–2), 201–218. https://doi.org/10.1016/S0012-821X(99)00051-5

Gardner, J. E., Ketcham, R. A., and Moore, G., 2013. Surface tension of hydrous silicate melts: Constraints on the impact of melt composition. *J. Volcanol. Geotherm. Res.* **267**, 68–74. https://doi.org/10.1016/j.jvolgeores.2013.09.007

Gardner, J. E., Wadsworth, F. B., Carley, T. L., Llewellin, E. W., Kusumaatmaja, H., and Sahagian, D., 2023. Bubble formation in magma. *Annu. Rev. Earth Planet. Sci.* **51**, 131–154. https://doi.org/10.1146/annurev-earth-031621-080308

Gonnermann, H. M., and Gardner, J. E., 2013. Homogeneous bubble nucleation in rhyolitic melt: Experiments and nonclassical theory. *Geochem. Geophys. Geosyst.* **14** (11), 4758–4773. https://doi.org/10.1002/ggge.20281

Hajimirza, S., Gonnermann, H. M., Gardner, J. E., and Giachetti, T., 2019. Predicting homogeneous bubble nucleation in rhyolite. *J. Geophys. Res. Solid Earth* **124** (3), 2395–2416. https://doi.org/10.1029/2018JB015891

Hajimirza, S., Gardner, J. E., and Gonnermann, H. M., 2022. Experimental demonstration of continuous bubble nucleation in rhyolite. *J. Volcanol. Geotherm. Res.* **421**, 107417. https://doi.org/10.1016/j.jvolgeores.2021.107417

Hamada, M., Laporte, D., Cluzel, N., Koga, K. T., and Kawamoto, T., 2010. Simulating bubble number density of rhyolitic pumices from Plinian eruptions: constraints from fast decompression experiments. *Bull. Volcanol.* **72** (6), 735–746. https://doi.org/10.1007/s00445-010-0353-z

Hamilton, D. L., Burnham, C. W., and Osborn, E. F., 1964. The solubility of water and effects of oxygen fugacity and water content on crystallization in mafic magmas. *J. Petrol.* **5** (1), 21–39. https://doi.org/10.1093/petrology/5.1.21

Hirth, J. P., Pound, G. M., and St Pierre, G. R., 1970. Bubble nucleation. *Metall. Trans.* **1** (4), 939–945. https://doi.org/10.1007/BF02811776

Hummel, F., Marks, P. L., and Nowak, M., 2024. Preparatory experiments to investigate the vesicle formation of hydrous lower Laacher See phonolite at near liquidus conditions. EGU General Assembly 2024, Vienna, Austria, EGU24-19758. https://doi.org/10.5194/egusphere-egu24-19758

Iacono-Marziano, G., Schmidt, B. C., and Dolfi, D., 2007. Equilibrium and disequilibrium degassing of a phonolitic melt (Vesuvius AD 79 “white

pumice") simulated by decompression experiments. *J. Volcanol. Geotherm. Res.* **161** (3), 151–164. https://doi.org/10.1016/j.jvolgeores.2006.12.001

Joswiak, M. N., Duff, N., Doherty, M. F., and Peters, B., 2013. Size-dependent surface free energy and Tolman-corrected droplet nucleation of TIP4P/2005 water. *J. Phys. Chem. Lett.* **4** (24), 4267–4272. https://doi.org/10.1021/jz402226p

Kelton, K. F., and Greer, A. L., 2010. Chapter 4 - Beyond the classical theory. In: Nucleation in condensed matter: Applications in materials and biology. Pergamon Materials Series **15**, 85–123. https://doi.org/10.1016/S1470-1804(09)01504-1

Le Gall, N., and Pichavant, M., 2016. Homogeneous bubble nucleation in H_2O- and H_2O-CO_2- bearing basaltic melts: Results of high temperature decompression experiments. *J. Volcanol. Geotherm. Res.* **327**, 604–621. https://doi.org/10.1016/j.jvolgeores.2016.10.004

Makhluf, A. R., Newton, R. C. and Manning, C. E., 2020. Experimental investigation of phase relations in the system $NaAlSi_3O_8$–H_2O at high temperatures and pressures: Liquidus relations, liquid-vapor mixing, and critical phenomena at deep crust-upper mantle conditions. *Contrib. Mineral. Petrol.* **175** (8), 76. https://doi.org/10.1007/s00410-020-01711-2

Marks, P. L., and Nowak M., 2024. Decoding the H_2O phase separation mechanism as the trigger for the explosive eruption of the Lower Laacher See phonolite. EGU General Assembly 2024, Vienna, Austria, EGU24-7723. https://doi.org/10.5194/egusphere-egu24-7723

Martel, C., and Schmidt, B. C., 2003. Decompression experiments as an insight into ascent rates of silicic magmas. *Contrib. Mineral. Petrol.* **144** (4), 397–415. https://doi.org/10.1007/s00410-002-0404-3

Marxer, H., Bellucci, P., and Nowak, M., 2015. Degassing of H_2O in a phonolitic melt: A closer look at decompression experiments. *J. Volcanol. Geotherm. Res.* **297**, 109–124. https://doi.org/10.1016/j.jvolgeores.2014.11.017

Moore, G., Vennemann, T., and Carmichael, I. S. E., 1998. An empirical model for the solubility of H_2O in magmas to 3 kilobars. *Am. Mineral.* **83** (1–2), 36–42. https://doi.org/10.2138/am-1998-1-203

Mourtada-Bonnefoi, C. C., and Laporte, D., 2004. Kinetics of bubble nucleation in a rhyolitic melt: an experimental study of the effect of ascent rate. Earth Planet. Sci. Lett. 218 (3–4), 521–537. https://doi.org/10.1016/S0012-821X(03)00684-8

Murase, T., and McBirney, A. R., 1973. Properties of some common igneous rocks and their melts at high temperatures. *Geol. Soc. Am. Bull.* **84** (11), 3563–3592. https://doi.org/10.1130/0016-7606(1973)84<3563:POSCIR>2.0.CO;2

Nishiwaki, M., and Toramaru, A., 2019. Inclusion of viscosity into classical homogeneous nucleation theory for water bubbles in silicate melts: Reexamination of bubble number density in ascending magmas. *J. Geophys. Res. Solid Earth* **124** (8), 8250–8266. https://doi.org/10.1029/2019JB017796

Ochs III, F. A., and Lange, R. A., 1999. The density of hydrous magmatic liquids. Science 283 (5406), 1314–1317. https://doi.org/10.1126/science.283.5406.1314

Paillat, O., Elphick, S. C., and Brown, W. L., 1992. The solubility of water in $NaAlSi_3O_8$ melts: a re-examination of Ab–H_2O phase relationships and critical behaviour at high pressures. *Contrib. Mineral. Petrol.* **112**, 490–500. https://doi.org/10.1007/BF00310780

Preuss, O., Marxer, H., Ulmer, S., Wolf, J., and Nowak, M., 2016. Degassing of hydrous trachytic Campi Flegrei and phonolitic Vesuvius melts: Experimental limitations and chances to study homogeneous bubble nucleation. *Am. Mineral.* **101** (4), 859–875. https://doi.org/10.2138/am-2016-5480

Sahagian, D., and Carley, T. L., 2020. Explosive volcanic eruptions and spinodal decomposition: A different approach to deciphering the tiny bubble paradox. *Geochem. Geophys. Geosyst.* **21** (6), e2019GC008898. https://doi.org/10.1029/2019GC008898

Schmelzer, J. W., and Baidakov, V. G., 2016. Comment on "Simple improvements to classical bubble nucleation models". *Phys. Rev. E* **94** (2), 026801. https://doi.org/10.1103/PhysRevE.94.026801

Shannon, R. D., 1976. Revised effective ionic radii and systematic studies of interatomic distances in halides and chalcogenides. *Acta Crystallogr. A: Found. Adv.* **32** (5), 751–767. https://doi.org/10.1107/S0567739476001551

Shea, T., 2017. Bubble nucleation in magmas: A dominantly heterogeneous process?. *J. Volcanol. Geotherm. Res.* **343**, 155–170. https://doi.org/10.1016/j.jvolgeores.2017.06.025

Sowerby, J. R., and Keppler, H., 2002. The effect of fluorine, boron and excess sodium on the critical curve in the albite–H_2O system. *Contrib. Mineral. Petrol.* **143** (1), 32–37. https://doi.org/10.1007/

s00410-001-0334-5

Sparks, R. S. J., 1978. The dynamics of bubble formation and growth in magmas: A review and analysis. *J. Volcanol. Geotherm. Res.* **3** (1–2), 1–37. https://doi.org/10.1016/0377-0273(78)90002-1

Stolper, E., 1982a. Water in silicate glasses: An infrared spectroscopic study. *Contrib. Mineral. Petrol.* **81** (1), 1–7. https://doi.org/10.1007/BF00371154

Stolper, E., 1982b. The speciation of water in silicate melts. *Geochim. Cosmochim. Acta* **46** (12), 2609–2620. https://doi.org/10.1016/0016-7037(82)90381-7

Tanaka, K. K., Tanaka, H., Angélil, R., and Diemand, J., 2016. Reply to "Comment on 'Simple improvements to classical bubble nucleation models'". *Phys. Rev. E* **94** (2), 026802. https://doi.org/10.1103/PhysRevE.94.026802

Tolman, R. C., 1949. The effect of droplet size on surface tension. *J. Chem. Phys.* **17** (3), 333–337. https://doi.org/10.1063/1.1747247

Toramaru, A., 1989. Vesiculation process and bubble size distributions in ascending magmas with constant velocities. *J. Geophys. Res. Solid Earth* **94** (B12), 17523–17542. https://doi.org/10.1029/JB094iB12p17523

Toramaru, A., 1995. Numerical study of nucleation and growth of bubbles in viscous magmas. *J. Geophys. Res. Solid Earth* **100** (B2), 1913–1931. https://doi.org/10.1029/94JB02775

Toramaru, A., 2001. A numerical experiment of crystallization for a binary eutectic system with application to igneous textures. *J. Geophys. Res. Solid Earth* **106** (B3), 4037–4060. https://doi.org/10.1029/2000JB900367

Toramaru, A., 2006. BND (bubble number density) decompression rate meter for explosive volcanic eruptions. *J. Volcanol. Geotherm. Res.* **154** (3–4), 303–316. https://doi.org/10.1016/j.jvolgeores.2006.03.027

Toramaru, A., 2022. Vesiculation and crystallization of magma: Fundamentals of volcanic eruption process, conditions for magma vesiculation. Springer Singapore. https://doi.org/10.1007/978-981-16-4209-8

Toramaru, A., and Kichise, T., 2023. A new model of crystallization in magmas: Impact of pre-exponential factor of crystal nucleation rate on cooling rate exponent and log-linear crystal size distribution. *J. Geophys. Res. Solid Earth* **128** (10), e2023JB026481. https://doi.org/10.1029/2023JB026481

Wagner, W., and Pruß, A., 2002. The IAPWS formulation 1995 for the thermodynamic properties of ordinary water substance for general and scientific use. *J. Phys. Chem. Ref. Data* **31** (2), 387–535. https://doi.org/10.1063/1.1461829

Zhang, Y., 1999. H_2O in rhyolitic glasses and melts: measurement, speciation, solubility, and diffusion. *Rev. Geophys.* **37** (4), 493–516. https://doi.org/10.1029/1999RG900012

CRediT authorship contribution statement

Mizuki Nishiwaki: Conceptualization, Methodology, Formal analysis, Investigation, Writing – Original Draft, Writing – Review & Editing, Visualization, Project administration, Funding acquisition.

Declaration of competing interest

The author declares that he has no known competing financial interests or personal relationships that could have appeared to influence the work reported in this paper.

Data availability

The author confirms that the data supporting the findings of this study are available within the article.